Multistage Crystallization of Plate-like Crystals: A Modeling and Experimental Study on Adipic Acid

Journal Article

Author(s):
Biri, Daniel; Jaeggi, Anna; Malach, Pavel; Rajagopalan, Ashwin Kumar [ID]; Mazzotti, Marco

Article

Multistage Crystallization of Plate-like Crystals: A Modeling and Experimental Study on Adipic Acid

Published as part of Crystal Growth & Design virtual special issue "Industrial Crystallization: ISIC 22/BACG 52".

Daniel Biri, Anna Jaeggi, Pavel Malach, Ashwin Kumar Rajagopalan, and Marco Mazzotti*

Cite This: https://doi.org/10.1021/acs.cgd.4c00277

Read Online

ACCESS | Metrics & More | Article Recommendations | SI Supporting Information

ABSTRACT: Particles exhibiting a plate-like shape, encountered during crystallization, present challenges in downstream processing. Consequently, it is crucial to manipulate the size and shape of such populations. However, comprehensive studies addressing this issue are lacking due to the absence of monitoring tools capable of accurately characterizing the particle size and shape distribution (PSSD) systems with a complex morphology. Leveraging recent advancements in monitoring technology, this work investigates a multistage crystallization process, encompassing growth, wet milling, and dissolution, to modify the PSSD of plate-like crystals. Employing a combination of experimental and modeling approaches, with adipic acid in water as the system, the influence of key multistage process parameters on the PSSD and filtration performance is evaluated. A multidimensional population balance equation-based model is utilized to analyze the intricate interplay among growth, dissolution, and breakage kinetics. The findings demonstrate the efficacy of the multistage process in modifying the particle size and fines content and thereby reducing the filter cake resistance of the product, a key indicator of powder processability. The insights gained from this study will be instrumental in designing processes for manipulating the size and shape of crystalline powders, particularly exhibiting a complex morphology like the one studied here.

Size and shape manipulation of plate-like crystals
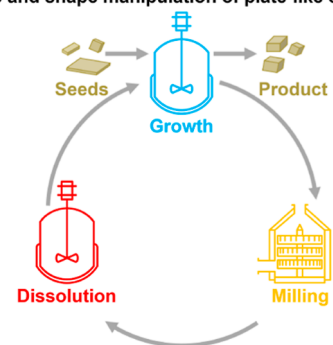
1. INTRODUCTION

Crystallization serves as a crucial and widespread purification step during the production of fine chemicals such as active pharmaceutical ingredients (APIs) and food additives. The processability of a product powder is intrinsically influenced by many characteristics exhibited at the particle scale.[1] Two primary determinants impacting the processability of a powder, the crystal size and the crystal shape, can be assessed through examination of the particle size and shape distribution (PSSD). The PSSD has a direct effect on critical product properties, such as filterability, powder flowability, bulk density, rate of dissolution, and compaction performance.[2−4] Inadequate processing characteristics of the powder can significantly increase the time and resources required for the development of a process capable of yielding a satisfactory product.[5,6]

Equant crystals are preferred over needle- or plate-like crystals due to the improved handling characteristics exhibited by their powders.[1,6] The majority of APIs do not crystallize as equant crystals, thus exhibiting an undesirable needle-like or plate-like morphology. For example, Ibuprofen and Aspirin crystallize as plate-like particles in specific solvents.[7,8] Powders consisting of plate-like particles tend to possess particularly unfavorable properties for downstream processing. Specifically, their filtration performance is very poor.[9−11]

Numerous techniques aimed at improving the PSSD have been reported.[12] Changes to the exhibited crystal morphology of small molecules have been successfully achieved through the use of various solvents[13] and additives.[14,15] Techniques such as spherical crystallization,[4] spherical agglomeration,[16] direct nucleation control,[17] temperature cycling,[18] and wet milling[19,20] have been employed successfully to alter both the size and the shape of crystals. Refined process strategies, combining temperature cycling and wet milling, have been successfully developed to manipulate populations of needle-like crystals of several different compounds.[21−23]

In contrast, there is a notable absence of systematic investigations into the design of crystallization processes for the size and shape manipulation of plate-like particles. This lack of studies can primarily be attributed to the inherent difficulty in accurately measuring the PSSD of plate-like crystals. Since no two crystals share the exact same geometry,
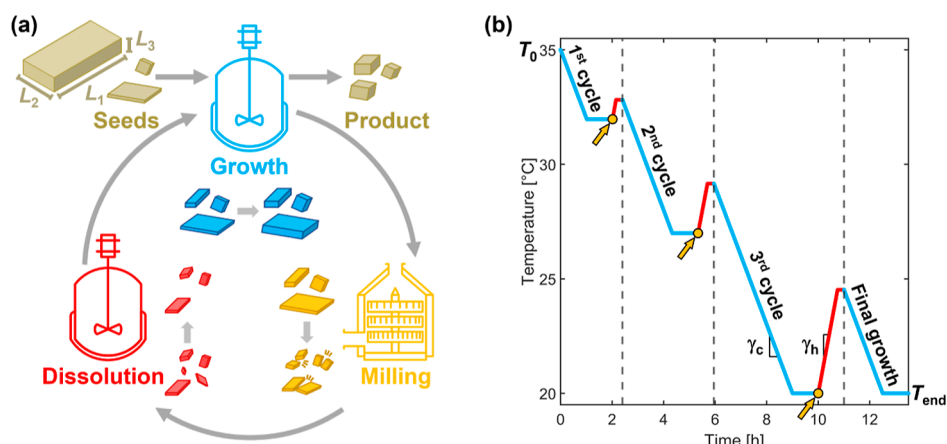
Figure 1. (a) Schematic plate-like particle with its three characteristic dimensions L_1, L_2, and L_3 as well as a process diagram of the multistage process. (b) Example temperature profile of a multistage process containing three cycles.

particle shapes need to be approximated using a generic particle model to obtain a PSSD. The actual geometry of plate-like crystals can be approximated using a generic particle model with a rectangular cuboid geometry, as shown in the top left corner of Figure 1a. This model describes particles using the three characteristic lengths L_1, L_2, and L_3. All characteristic dimensions are assumed to be perpendicular to one another, and thus, the particle volume is approximated by their product.

A recently introduced characterization framework for plate-like particle populations has addressed the challenge of characterizing plate-like particles by utilizing stereoscopic imaging, advancements in machine learning, and innovative manufacturing techniques. The accuracy of the technique has been experimentally assessed.[24,25] Capitalizing on these advancements, this study represents the first systematic exploration into manipulating the PSSD of plate-like crystals through a multistage crystallization process comprising growth, wet milling, and dissolution stages. The crystallization of adipic acid, the model compound of this work, has already been subject to previous investigations, which have, however, focused either on the development of continuous crystallization processes[26] or on the evolution of single crystals.[27]

Developing crystallization processes through experimental investigations alone is time-consuming and resource-intensive. A population balance equation (PBE) model can help in gaining an understanding of the dominant phenomena in a specific crystallization process. These models also allow for a quick and efficient assessment of the effects of and the interactions between different process parameters and compound properties.[28] This can reduce the number of experiments required to identify an adequate crystallization process.[23] PBE models have been successfully used to simulate the evolution of needle-like particles through growth, dissolution, and breakage.[20,29−35]

In this work, we evaluate the effectiveness of a multistage cooling crystallization process, incorporating growth, wet milling, and dissolution in altering the PSSD of plate-like crystals, illustrated in Figure 1. To understand the capabilities and limitations of the process, the results of an experimental campaign are combined with the insights gained from a simulation study.

The novelty of this work lies in

- the assessment of the impact of a multistage crystallization process on the PSSD of plate-like crystals through an experimental campaign;
- the evaluation of the downstream processability through filtration performance measurements of the product consisting of plate-like crystals;
- the utilization of a morphological PBE modeling framework for plate-like particles to study the evolution of the PSSD and the impact of process and compound properties on the crystallization process outcome.

This article is divided into six sections. After explaining the conceptual design of the multistage crystallization process in Section 2, the experimental campaign using adipic acid as a model compound is described in Section 3. This is then followed up in Section 4, where a new morphological PBE model is used to study the effects of the process parameters and of compound properties on the region of attainable product PSSDs. The experimental and computational results are subsequently compared and analyzed to infer the properties of the model compound. Finally, in Section 5, the capabilities and limitations of the process are discussed, and conclusions are drawn.

2. PROCESS DESIGN

The multistage crystallization process investigated in this work comprises three distinct stages, namely, growth, wet milling, and dissolution, as illustrated in Figure 1a. The arrangement of the stages follows a previously reported rationale.[30]

The temperature dependence of the solubility is exploited to drive crystallization. Consequently, if the process is initiated at equilibrium conditions, yield is defined as the difference in solubility between the initial process temperature, T_0, and the final process temperature, T_{end}. An exemplary temperature profile of the multistage process is shown in Figure 1b.

The growth stage is inherently indispensable in a crystallization process as it delivers its fundamental service: incorporating solute molecules into the solid crystals. The growth kinetics of the crystal faces determines the final crystal morphology, which, as is the case with plate-like crystal shapes, can be undesirable.

To mechanically reduce the aspect ratios of the crystals, a rotor-stator wet mill is employed in the second stage of the process to cause crystal breakage. The aspect ratio, ϕ_{ij}, is

defined as the ratio between the characteristic particle dimensions, L_i and L_j, with $L_i > L_j$.

Wet milling tends to generate broad distributions containing significant fractions of fines, which leads to undesirable product powder properties.[36] In this work, fines are defined as particles with a volume smaller than that of a cube with a side length of 40 μm. The partial dissolution step in the third stage completely dissolves the fines while shrinking the larger particles.

The number of cycles of growth, milling, and dissolution, n_C, is a process parameter. An equivalent fraction of the final yield is crystallized in every cycle. The end temperatures of the dissolution stages are selected to dissolve a predefined fraction of the mass theoretically crystallized if the process had reached equilibrium after the preceding growth stage. This approach to defining the temperatures of the different stages has been reported previously.[37] Upon completion of the specified number of cycles, a final growth stage is performed to reach the final process temperature, T_{end}.

In previous works, when applying the multistage process to needle-like particles, three key process parameters were identified as controlling the process outcome. These are the number of cycles, n_C, the rotor speed of the wet mill, i.e., the milling intensity, θ, and the fraction of mass dissolved during each dissolution stage, m_D. Changes to other parameters, such as the cooling and heating rates, have a smaller impact on process outcomes.[22]

3. EXPERIMENTAL INVESTIGATION

3.1. Materials. Aqueous solutions of adipic acid (Sigma-Aldrich, purity ≥99%) are used in all experiments. Deionized and microfiltered water is obtained from a Milli-Q Advantage A10 unit (Millipore, Zug, Switzerland). While adipic acid does not crystallize in a rectangular cuboid shape in pure water,[38] such a geometry can be obtained by introducing 1 wt % of the copolymer Pluronic F127 (Sigma-Aldrich, Switzerland). The smooth crystal surfaces and rectangular contours of such adipic acid crystals are evident in the micrograph in Figure 2b. The additive Pluronic F127 has already been studied to modify the morphology of succinic acid,[39,40] which, like adipic acid, is a linear saturated dicarboxylic acid.

3.2. Experimental Setup. All experiments are performed in a 2 L jacketed glass crystallizer (LaboTechSystems LTS, Reinach, Switzerland). The suspensions are stirred using a four-blade glass impeller
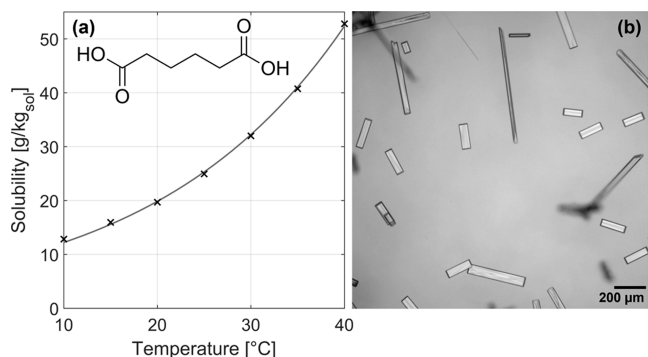
with a diameter of 60 mm and 45° inclined blades (LaboTechSystems LTS AG, Reinach, Switzerland), which is driven by an overhead stirrer (Eurostar digital, IKA-Werke GmbH & Co. KG, Staufen, Germany). The temperature is controlled via an oil bath (Huber Pilot ONE, Offenburg, Germany). To verify the absence of nucleation during the crystallization, the ParticleTrack G400 (Mettler Toledo, Switzerland), a focused beam reflectance measurement system, is employed. For milling, the crystallizer is first drained into a stirred 2 L glass beaker. Subsequently, the suspension is pumped back into the crystallizer through a wet mill (Magic Lab, module DR, generators 2G-4M-6F, IKA-Werke GmbH & Co. KG, Staufen, Germany) using a peristaltic pump (Ismatec, Wertheim, Germany).

3.3. Solubility Measurements. To design the temperature profile of the crystallization process as described in Section 2, the solubility of adipic acid in an aqueous solution containing 1 wt % Pluronic F127 is measured gravimetrically between 10 and 40 °C. The solubility measurements were repeated six times, with the coefficient of variation always being lower than 2.5%, at each specified temperature. The mean solubility at each temperature is shown in Figure 2a. The experimental data are used to estimate the parameters of the exponential equation

$$c^*(T) = k_{S,1}\exp(k_{S,2}T) \tag{1}$$

where $c^*(T)$ denotes the solubility of adipic acid [g/kg$_{sol}$] at temperature T [K] and the two estimated parameters are $k_{S,1} = 1.33 \times 10^{-5}$ g kg$_{sol}^{-1}$ and $k_{S,2} = 4.85 \times 10^{-2}$ K^{-1}.

Pluronic F127 has been shown to increase the solubility of certain small organic compounds in aqueous solutions.[41] The reported solubility of adipic acid in pure water is roughly 6% lower than the one measured in this work in an aqueous solution containing 1 wt % Pluronic F127.[42,43]

3.4. Preparation of Seed Crystals. A single batch of adipic acid seed crystals is used throughout the experimental campaign to ensure that the initial PSSD is always the same.

The seeds are produced via seeded cooling crystallization. For this, 180 g of adipic acid and 1.8 g of Pluronic F127 are dissolved in 1800 g of deionized water at 55 °C. The suspension is brought to 50 °C, and 2.0 g of adipic acid is added as seeds. The suspension is then continuously circulated through the wet mill running at 16,000 rpm with a flow rate of 1 L min^{-1} for 2 min. The suspension is subsequently cooled to 30 °C at a rate of 10 K h^{-1} before being milled a second time the same way as described before. The suspension is further cooled to 20 °C over 180 min before milling at 12,000 rpm. Finally, this suspension is filtered and washed using a mixture of 70/30 wt %/wt % toluene/acetone to yield around 90 g of adipic acid seeds.

3.5. Design of the Experimental Campaign. The design space of the experimental campaign is chosen to explore a wide range of process conditions. For the three critical process parameters (the number of cycles, n_C, the mass dissolved per cycle, m_D, and the milling intensity, θ), a set of parameter values are defined based on the experience gained from applying the multistage process to needle-like crystals.[22,31,37] For both n_C and θ, two values are used. For m_D, three values are chosen, going from no dissolution to a large fraction of dissolved mass. The parameter values are reported in Table 1. All possible combinations of these process parameters yield 12 parameter sets, with 10 used for experimental purposes, as detailed in Table 3 in Section 3.7. Notably, two sets of process parameters with a high milling intensity ($\theta = 24{,}000$ rpm) and no dissolution ($m_D = 0$) are excluded. Achieving no dissolution during high-intensity wet milling is experimentally very challenging due to the intense heating caused by the wet mill. While some increase in temperature is not an issue for the experiments where wet milling is deliberately followed by some dissolution, it notably impacts experiments designed without dissolution.

The remaining process parameters are kept constant for all experiments to reduce the size of the design space. At the end of all experiments, the suspension is passed through the mill running at a low milling intensity of 6000 rpm to deagglomerate the roughly 10%

Figure 2. (a) Chemical formula of adipic acid as well as its gravimetrically measured solubility in water containing 1 wt % Pluronic F127. The coefficient of variation for all solubility measurements is lower than 2.5%. The experimental data are used to fit an exponential function, as described in Section 3.3. (b) Micrograph of adipic acid crystals suspended in a saturated aqueous solution containing 1 wt % Pluronic F127.

Table 1. Experimental Conditions and Process Parameters Used for the Experimental Campaign

fixed operating conditions	
initial temperature T_0	35°C
final temperature T_{end}	20°C
seed mass m_0	2 g kg^{-1}
solvent mass	1800 g
initial solute mass	72.9 g
expected yield	22.33 g kg^{-1}
growth stage	
cooling rate γ_c	3 K h^{-1}
holding time after growth $t_{h,G}$	120 min
milling stage	
pump flow rate F	1 L min^{-1}
dissolution stage	
heating rate γ_h	6 K h^{-1}
holding time after dissolution $t_{h,D}$	15 min
variable process conditions	
number of cycles n_C	[2, 4]
milling intensity θ	[12, 24] $\times 10^3$ rpm
mass fraction dissolved m_D	[0, 0.2, 0.4]

agglomerated particles present in the final populations. Note that, as shown in a dedicated experiment in Section S1.2 in the Supporting Information, the low milling intensity during deagglomeration induces no further breakage of the primary particles. Then, the suspension is filtered and washed with a 70/30 wt %/wt % toluene/acetone solution before drying in an oven at 60 °C for 4 h.

3.6. Product Characterization. *3.6.1. Product PSSD Measurement.* For the analysis of particle size and shape, a previously reported stereo imaging device, referred to as the Dual Imaging System for Crystallization Observation, in short *DISCO*, is employed.[44] The particle contours acquired using the cameras from the imaging device undergo characterization through an analysis workflow, which first classifies them into different categories, to exclude agglomerates and air bubbles, and then characterizes plate-like particles individually, utilizing an artificial neural network to obtain accurate measurements of the length, L_1, width, L_2, and thickness, L_3, with $L_1 > L_2 > L_3$.[24] Recently, the accuracy and precision of this characterization technique were assessed using populations of uniform polymer particles exhibiting a plate-like geometry. These particles were of a similar size and shape as the particles observed in this work. Therefore, the measurement accuracy in this study is roughly 10 μm for all three characteristic dimensions.[25]

The PSSD of each crystallized product in this study is evaluated by transferring between 50 and 100 mL of the final suspension into a second 2 L vessel containing a saturated aqueous solution of adipic acid with 1 wt % Pluronic F127, emulating the composition of the liquid phase at the end of the process. This dilution of the suspension ensures minimal overlap of particles in the images and facilitates an accurate characterization of the individual particles. The number of particles characterized to ensure an accurate representation of the PSSD is between 250,000 and 500,000 crystals. This is an order of magnitude higher compared to previous studies for needle-like particles.[31] This is needed to ensure a similar density, hence similar granularity, in the state space occupied by the particles, which is two-dimensional in the case of needle-like particles and three-dimensional in the case of plate-like particles.

In this work, to facilitate the comparison between different PSSDs, populations of particles are often described by using different average characteristics. While containing less information than the PSSD itself, this reduction is essential for comprehension. The characteristics used in this work can be found in Table 2 and are defined using the moments of the population. The moment μ_{ijk} of a PSSD $[\mu m^{i+j+k}$ kg$_{sol}^{-1}]$ is defined as

Table 2. Volume-Weighted Characteristics Used to Compare the Mean Characteristic Lengths of Different Populations

mean characteristic length	definition
$L_{1,v}$ $[\mu m]$	μ_{211}/μ_{111} $[\mu m]$
$L_{2,v}$ $[\mu m]$	μ_{121}/μ_{111} $[\mu m]$
$L_{3,v}$ $[\mu m]$	μ_{112}/μ_{111} $[\mu m]$

$$\mu_{ijk}(t) = \int_0^\infty \int_0^\infty \int_0^\infty f(L_1, L_2, L_3, t) L_1^i L_2^j L_3^k dL_1 dL_2 dL_3 \tag{2}$$

where f represents the number density function of the PSSD $[\mu m^{-3}$ kg$_{sol}^{-1}]$. The indices i, j, and k stand for the order of the moment with respect to the characteristic lengths L_1, L_2, and L_3, respectively.

3.6.2. Product Filter Cake Resistance Measurement. To assess the impact the modification of the PSSD has on the product properties, the filter cake resistance of the crystallized product is measured for all experiments by performing vacuum filtration. This resistance is calculated using a mass-normalized version of Darcy's law[45]

$$\alpha_m = \left(\frac{\Delta P A}{Q_v \mu} - \beta \right) \frac{A}{m_c} \tag{3}$$

where α_m is the filter cake resistance $[m\ kg^{-1}]$, ΔP is the pressure drop over the cake $[Pa]$, A is the filtration area $[m^2]$, Q_v is the volumetric flow rate $[m^3\ s^{-1}]$, μ is the dynamic viscosity $[Pa\ s]$, and m_C is the mass of the filter cake $[kg]$. The parameter β is the blank resistance $[m^{-1}]$, which can be calculated by measuring the flow rate through the filtration setup in the absence of a filter cake and using

$$\beta = \frac{\Delta P A}{Q_v \mu} \tag{4}$$

As the solubility of adipic acid varies significantly with temperature in many commonly used solvents, the filter cake undergoes uncontrolled growth or dissolution during filterability measurements. This reproducibility issue is overcome by using a low-viscosity silicone oil (Thermofluid SilOil M20.195/235.20, Peter Huber Kältemaschinenbau SE, Offenburg, Germany), in which adipic acid exhibits negligible solubility. The procedure for measuring the filter cake resistance starts by suspending 10.0 g of the product powder in 50 mL of silicone oil. Then, the suspension is filtered through MN 615 filter paper (MACHEREY-NAGEL AG, Oensingen, Switzerland) to build a filter cake in a Büchner funnel (Haldenwanger 127C, Peter Huber Kältemaschinenbau SE, Offenburg, Germany) with a surface area of 14.4 cm². Following cake formation, 1500 mL of the silicone oil is passed through the cake, and the time required for every 100 mL of the liquid to pass through the filter cake is recorded. To maintain a constant pressure difference of 800 mbar throughout the entire measurement, a vacuum controller (V-800, Büchi Labortechnik AG, Flawil, Switzerland) is employed. The measurements have been repeated for most product powders, and they show good reproducibility. The mean flow rate is used to calculate the filter cake resistance.

3.7. Experimental Results. *3.7.1. Effect of the Critical Process Parameters on the PSSD.* The results from ten different crystallization experiments are reported in Table 3. This includes the parameters defining each process, the volume-weighted average characteristic lengths of the product population, and the mean filter cake resistance of the products.

The average characteristic lengths from Table 3 are visualized in Figure 3, with Figure 3a showing the different product populations in the L_1-L_2-plane and Figure 3b showing the populations in the L_1-L_3-plane. The solid lines in the two panels denote $L_1 = L_2$ and $L_2 = L_3$. The dashed lines represent particles with a specific aspect ratio, namely, $\phi_{12} = 10/3$ and $\phi_{13} = 10$, respectively. With reference to Figure 3, it can be observed that the product populations are all distributed along the aforementioned dashed lines, and consequently, all have similar aspect ratio values. The average volume-weighted

Table 3. List of Population Number, the Three Critical Process Parameter Values (the Fraction of Mass Dissolved, m_D, Number of Cycles, n_C and Milling Intensity, θ), as Well as the Resulting Volume-Weighted Mean Average Sizes and the Filter Cake Resistance of the Product Powder, α_m

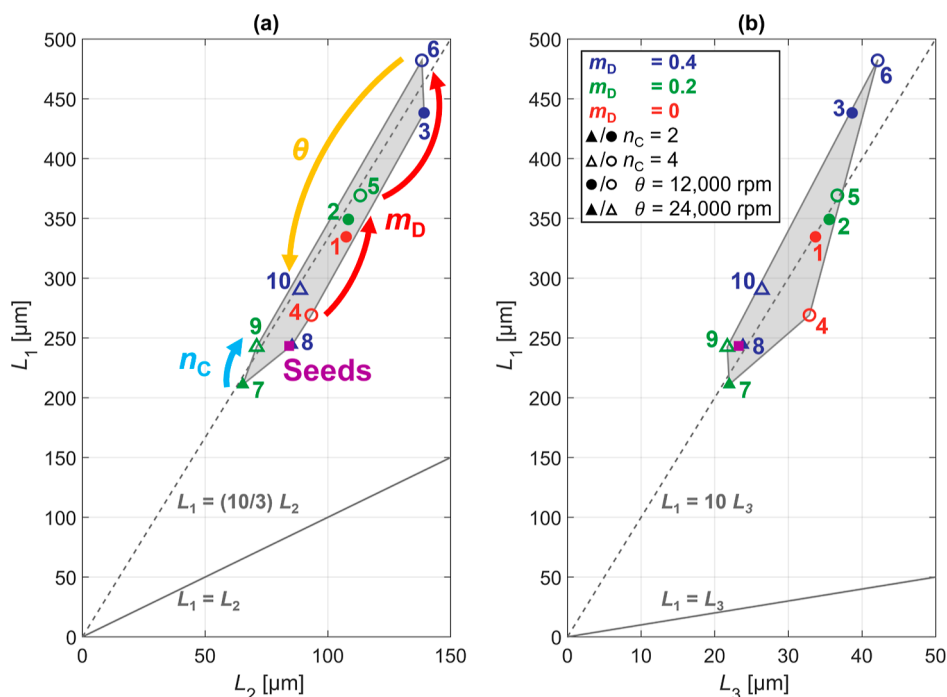| population	$m_D\ [-]$	$n_C\ [-]$	$\theta\ [10^3\ \text{rpm}]$	$L_{1,v}\ [\mu m]$	$L_{2,v}\ [\mu m]$	$L_{3,v}\ [\mu m]$	$\alpha_m\ [10^7\ \text{m kg}^{-1}]$
1	0	2	12	340	110	30	6.4
2	0.2	2	12	350	110	40	4.3
3	0.4	2	12	440	140	40	3.7
4	0	4	12	270	90	30	8.0
5	0.2	4	12	370	110	40	2.6
6	0.4	4	12	480	140	40	0.8
7	0.2	2	24	210	70	20	7.2
8	0.4	2	24	240	90	20	6.0
9	0.2	4	24	240	70	20	9.4
10	0.4	4	24	290	90	30	6.1

Figure 3. Visualization of the volume-weighted mean lengths of the different product populations on the L_1-L_2-plane in (a) and on the L_1-L_3-plane in (b). Both panels contain a solid line indicating a shape with all characteristic dimensions being of the same size. The dashed line in each panel represents an aspect ratio of $\phi_{12} = (10/3)$ and $\phi_{13} = 10$, respectively.

characteristic lengths of the different product populations differ at most by a factor of two.

3.7.1.1. Milling Intensity θ. A clear difference in average size, depending on the milling intensity, can be observed. Processes employing a high milling intensity ($\theta = 24{,}000$ rpm; populations 7 to 10) produce populations with considerably smaller average characteristic lengths compared to processes with lower milling intensity ($\theta = 12{,}000$ rpm; populations 1 to 6). It can also be observed that varying the process parameters n_C and m_D changes the average size of the product population less at high milling intensities ($\theta = 24{,}000$ rpm) compared to the cases at low-intensity milling ($\theta = 12{,}000$ rpm). Intense breakage seems to prevail over the differences due to more cycles or more fines removal. The milling intensity, θ, is the process parameter with the biggest impact on the particle sizes, as highlighted in Figure 3a with a yellow arrow.

3.7.1.2. Fraction of Mass Dissolved m_D. Populations produced with larger fractions of mass dissolved per cycle, m_D, have larger average particle sizes. This effect is most visible for the PSSDs produced with $n_C = 2$ and $\theta = 12{,}000$ rpm, as highlighted in Figure 3a with two red arrows. This effect is expected as a higher m_D leads to the

removal of more fines, causing the solute to crystallize on fewer particles during growth, thereby increasing their average size.

3.7.1.3. Number of Cycles n_C. It is worth noting that the effect of the number of cycles n_C on the product population depends on the fraction of mass dissolved per cycle, m_D. More wet milling without fines removal, $m_D = 0$, leads to a decreasing particle size. In contrast, at $m_D = 0.2$, a small increase in the particle size with a higher number of cycles can be observed. Even more notable are the significant increases in particle size observed at $m_D = 0.4$.

3.7.1.4. Combined Effects and Conclusions. Referring to Figure 4a, a positive correlation between mass dissolved per cycle, m_D, and average aspect ratio, ϕ_{13}, of the product crystals can be observed. It is unclear if either the growth or the dissolution kinetics cause this rather clear effect, and further investigation would be required. The other two process parameters, i.e., n_C and θ, do not correlate with the aspect ratio.

While no dissolution, i.e., $m_D = 0$, results in the lowest aspect ratio, dissolution remains important to reduce the fraction of fines in the product crystals. Figure 4b shows the mass fraction of fines present in the product as a function of the mass dissolved, m_D. A clear trend can be observed, with the product fines content reducing as the mass
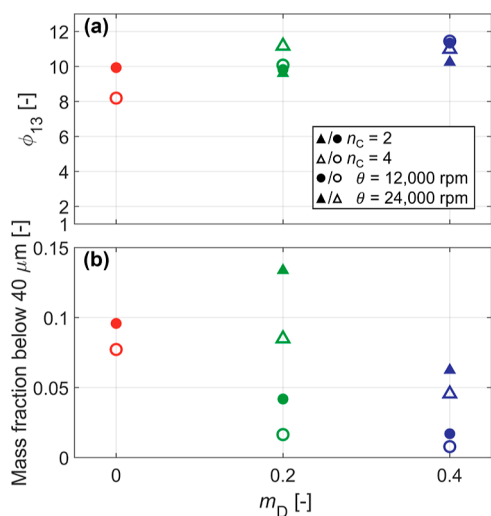
Figure 4. (a) Volume-weighted mean aspect ratio ϕ_{13} of the product PSSDs as a function of the mass dissolved per cycle, m_D, used to produce the populations. (b) Mass fraction of particles with a volume smaller than a cube with a side length of 40 μm. The circles and triangles represent milling intensities of 12,000 and 24,000 rpm, respectively. Full symbols represent $n_C = 2$ and empty symbols represent $n_C = 4$.

dissolved, m_D, increases. Furthermore, it can be observed that increasing the number of cycles, n_C, leads to a decrease in the fraction of fines and that increasing the milling intensity, θ, leads to an increased fraction of fines under all conditions investigated.

Concluding, the milling intensity, θ, has a significant impact on the average particle size and on the fraction of fines in the final product. The number of cycles, n_C, leads to an increase or decrease of the average particle size depending on the fraction of mass dissolved per cycle, m_D. The third key process parameter, m_D, has a slight influence on the average particle shape but mainly determines the fraction of fines in the final product.

3.7.2. Filter Cake Resistance of the Product Powder. The filter cake resistances of all the product powders, measured according to the

protocol described in Section 3.6.2, are presented in the last column of Table 3 and visualized in Figure 5, where the volume-weighted average particle sizes of the populations are shown in the L_1–L_3 plane, as in Figure 3b. The colors of the symbols indicate the mean measured filter cake resistance, going from green for the lowest measured resistance to red for the highest measured resistance.

With reference to Figure 5a, one can observe a general correlation indicating that an increase in the average particle size of powders reduces their filter cake resistance. An exception to this trend is, for example, population 4 when compared to population 8, where the former possesses a larger average particle size yet exhibits a higher filter cake resistance. This deviation can be explained by comparing the marginal distributions of their PSSDs, visualized in Figure 5b. A marginal distribution is the projection of the volume-weighted particle density function onto a coordinate plane. Population 4, with its broad PSSD, contains a significant fraction of fines and is the product of a process with $m_D = 0$, $n_C = 2$, and $\theta = 12,000$ rpm. The more compact distribution of Population 8 contains fewer fines and results from a process with $m_D = 0.4$, $n_C = 2$, and $\theta = 24,000$ rpm.

Confirming this observation, Figure 6a shows a clear positive correlation between fines and filter cake resistance. Figure 6b presents a negative correlation between the filter cake resistance and the mass dissolved per cycle under all conditions.

These findings clearly demonstrate that while it is an important indicator, the average particle size is not the sole metric influencing filter cake resistance. Furthermore, the results underscore the value that the multistage crystallization process adds compared to simpler processes that do not dissolve fines. The highest filter cake resistances are observed for processes during which milling is conducted without adequate fines removal. As the average aspect ratios of all populations are similar, no conclusion can be drawn about the impact of particle shape manipulation on filter cake resistance.

4. MODELING AND SIMULATIONS

4.1. Process Modeling. By creating a modeling framework capable of simulating the evolution of the PSSD of plate-like crystals through the multistage crystallization process, the effects of the three key process parameters and their interactions can be rationalized. This provides context to the
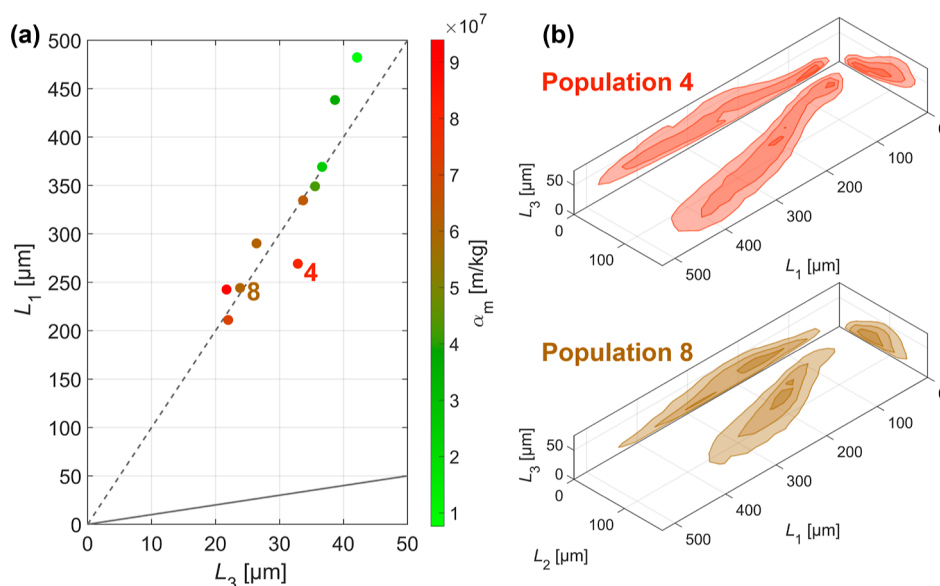

Figure 5. (a) Volume-weighted mean lengths of the different product populations in the L_1–L_3 plane as well as the mass-specific filter cake resistance using a color gradient. The gradient goes from green for the lowest measured filter cake resistance to red for the highest measured resistance. (b) Volume-weighted 3D marginal distributions of populations 4 and 8. The contour areas enclose 90, 50, and 10% of the total particle volume, respectively.
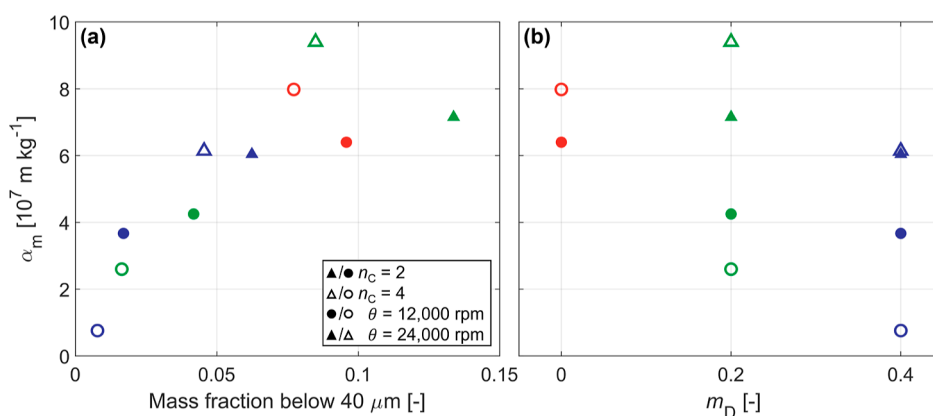
Figure 6. (a) Correlation between the filter cake resistance, α_m, and the mass fraction of particles with a volume smaller than a cube with a side length of 40 μm. (b) Visualization of the filter cake resistance, α_m, versus the mass dissolved, m_D.

experimental findings and gives insight into the optimal process design based on specific compound characteristics.

To accurately describe the particles and their evolution, an appropriate model must not only capture key fundamental phenomena but also be based on a generic particle model capable of describing the size and morphology of the particles of interest. While particle models with a single characteristic length can be employed to describe particles with complex symmetries, this is associated with a substantial error if the shape of the particles evolves during the process. Needle-like particles require two characteristic lengths to be accurately described. The error associated with using a model with one characteristic length only to describe needles has been assessed and discussed previously.[46] Given the morphology of plate-like crystals, such as the rectangular cuboid shape studied in this work, an accurate description necessitates a minimum of three characteristic lengths. A distinct multidimensional PBE model using three characteristic lengths is employed for each stage of the process to best simulate the relevant phenomena.

4.1.1. Growth and Dissolution Models. The morphological PBE used to describe the evolution of a population during growth and dissolution in a well-mixed batch crystallizer can be written as follows[24]

$$\frac{\partial f}{\partial t} + \sum_{i=1}^{3} \left(\Gamma_i \frac{\partial f}{\partial L_i} \right) = 0 \tag{5}$$

where f is the number density function $[\mu\mathrm{m}^{-3}\,\mathrm{kg}_{\mathrm{sol}}^{-1}]$ and Γ_i is the growth or dissolution rate $[\mu\mathrm{m}\,\mathrm{s}^{-1}]$ along the characteristic particle length i. This model neglects breakage, agglomeration, and nucleation. By coupling to the mass balance, the PBE model ensures the conservation of mass. The model is solved using a high-resolution finite volume method, incorporating a van Leer flux Limiter to eliminate oscillations caused by discontinuities in the number density function.[29] In Section S2.1 in the Supporting Information, a more detailed description of the growth and dissolution models, containing all relevant equations, as well as the initial and boundary conditions, can be found.

4.1.2. Breakage Model. To simulate breakage during the wet milling stage, a model for plate-like crystals is developed, inspired by an earlier breakage model for needle-like particles.[32]

Particles after breakage must exhibit geometric similarity with particles before breakage; otherwise, the assumption that all particles can be accurately described using a generic cuboid particle model would be invalid. Consequently, breakage events are assumed to occur exclusively along a plane orthogonal to one of the characteristic directions of the particles. It is assumed that each breakage event involves one particle breaking into two new crystals. Growth, dissolution, and agglomeration are neglected during the wet milling stage.

$$\frac{\mathrm{d}f(\tau, \underline{L})}{\mathrm{d}\tau} - \sum_{i=1}^{3} (B_i(a, \underline{L}) - E_i(a, \underline{L})) = 0 \tag{6}$$

The residence time in the wet mill is denoted as τ [s]. B_i and E_i denote the birth and death terms along the characteristic length i, respectively. The birth term represents the creation of new particles at size $\underline{L}$ during a breakage event, while the death term accounts for the disappearance of particles of the same size due to breakage.

The two expressions characterizing the birth and death terms are the breakage frequency and daughter distribution. The breakage frequency considers the effects of the operating conditions of the rotor-stator wet mill, particle size, and particle shape. The functional form draws inspiration from a study on the breakage of needle-like particles.[32] Depending on the dominating breakage mechanism, the daughter distribution can take different functional forms. In this work, a uniform probability is used, where all sizes of daughter crystals are equally likely to occur. The breakage PBE model is solved using the fixed pivot method[47] to guarantee the preservation of mass and the creation of an additional particle per event. The breakage model is described in detail in Section S2.2 in the Supporting Information.

4.2. Reference Simulation. To gain a general understanding of the evolution of the PSSD throughout the multistage crystallization process, a simulation using a reference set of operating conditions and compound-specific properties has been analyzed. The operating conditions and process parameters used for the reference simulation can be found in Table 4.

The reference set of kinetic parameter values can be found in Table S3 in the Supporting Information. In the reference simulation, the linear growth kinetic parameters k_1^G and k_2^G are modified, i.e., $k_1^\mathrm{G} = 5k_{\mathrm{ref}}^\mathrm{G}$ and $k_2^\mathrm{G} = \sqrt{5}k_{\mathrm{ref}}^\mathrm{G}$, to ensure that growth is the fastest for L_1 and the slowest for L_3.

The three-dimensional grid used to discretize the PSSD contains 80, 60, and 30 bins along L_1, L_2, and L_3, respectively. This results in a grid containing 144,000 voxels. The grid is

G

Table 4. List of the General Operating Conditions and the Specific Operating Conditions for the Three Different Types of Stages

general	number of cylces	n_C	[—]	4
	rotor speed	θ	[10^3 rpm]	24
	fraction of mass dissolved per cycle	m_D	[—]	0.4
	initial temperature	T_0	[°C]	35
	final temperature	T_{end}	[°C]	20
	seed mass	m_0	[g/kg$_{sol}$]	2
growth stage	cooling rate	γ_c	[K h^{-1}]	3
	hold after cooling	$t_{h,G}$	[min]	120
milling stage	residence time in the wet mill	τ	[s]	4
dissolution stage	heating rate	γ_h	[K h^{-1}]	6
	hold after heating	$t_{h,D}$	[min]	15

defined for 0 μm < L_1 < 800 μm, 0 μm < L_2 < 600 μm, and 0 μm < L_3 < 300 μm. All simulations are performed on a desktop computer with an Intel Core i7-1065G7 CPU@1.30 GHz with 4 cores and 16 GB of RAM using MATLAB.

To ensure a more direct comparison between the experiments and the simulations, the seed PSSD for all simulations is the measured population of seeds used during the experimental campaign, as described in Section 3. A more detailed description of the seed PSSD can be found in Section S1.1 in the Supporting Information.

Figure 7 provides an overview of the evolution of some of the key metrics of the population throughout the reference simulation. Figure 7a illustrates the temperature profile. Referencing Figure 7b, changes in the PSSD can be assessed
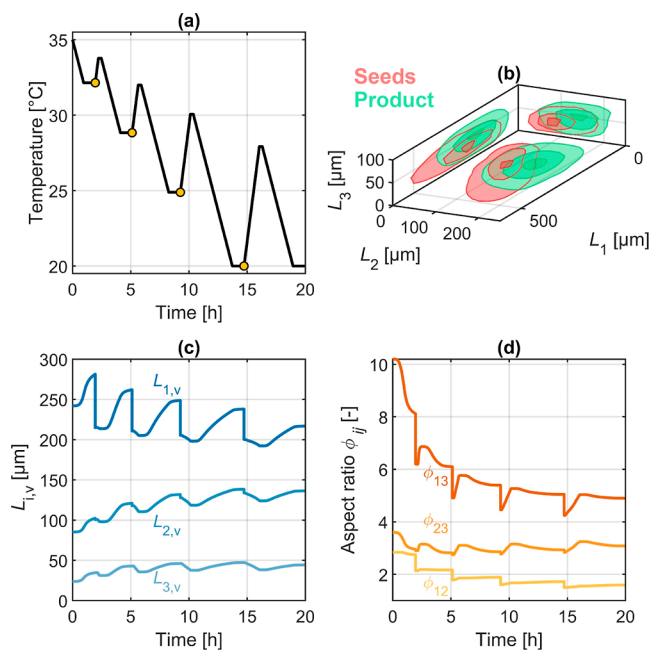

Figure 7. (a) Temperature evolution, the milling events are marked with a yellow dot. (b) Marginal distributions of the seed and product PSSD (in red and green, respectively). The contour areas enclose fractions 0.9, 0.5, and 0.1 of the total particle volume. (c) Evolution of $L_{1,v}$, $L_{2,v}$ and $L_{3,v}$ (with progressively lighter colors). (d) Evolution of the aspect ratios ϕ_{13}, ϕ_{23}, and ϕ_{12} (with progressively lighter colors). This simulation was run with n_C = 4, θ = 24,000, and m_D = 0.4.

qualitatively using the marginal distributions of the initial (red) and final (green) populations. Figure 7c tracks the shift in volume-weighted mean characteristic lengths, showing an increase during the growth phases, a decrease while milling, and minimal changes during dissolution. Figure 7d displays the changes in aspect ratio throughout the process. During growth and milling, the aspect ratios decrease. The decrease during milling is reflective of breakage across the longest characteristic length being the most likely. This follows from the proportional parameters for breakage being the same for all characteristic lengths and the breakage kernel containing a dependence on the absolute length. The increase in aspect ratio during dissolution is explained by the fact that the smaller characteristic lengths undergo a faster relative reduction in their size compared to the larger characteristic lengths as the dissolution rates along all characteristic lengths are the same. Looking at the initial and the final PSSD, the aspect ratios ϕ_{13} and ϕ_{12} are significantly reduced, thus demonstrating that for this set of rate parameters, the multistage process can effectively alter the PSSD of plate-like particles.

4.3. Parametric Study. Simulating different crystallization processes by varying the three key process parameters, the number of cycles, n_C, the milling intensities, θ, and the mass dissolved per cycle, m_D, helps to assess the effect of process conditions for a given set of compound properties. Using all possible permutations of the key process parameter values listed in Table 5 results in 30 distinct crystallization processes per set of compound properties.

Table 5. List of All Values Used for the Different Key Operating Parameters in the Parametric Study, Namely, the Number of Cycles, n_C, the Milling Intensities, θ, and the Mass Dissolved Per Cycle, m_D

number of cycles	n_C	[—]	[2−6]
rotor speed	θ	[10^3 rpm]	[12, 18, 24]
fraction of mass dissolved per cycle	m_D	[—]	[0, 0.2, 0.4]

The kinetic rate expressions for growth, breakage, and dissolution linearly depend on parameters k_i^G, k_i^B, and k_i^D, respectively, with i denoting the different characteristic lengths. These parameters are obtained by multiplying the reference kinetic values k_{ref}^G, k_{ref}^B, and k_{ref}^D, listed in Table S3 in the Supporting Information, using scaling factors. Three sets of scaling factors are used for each of the three phenomena, as listed in Table 6, creating 27 individual scenarios.

The kinetic scaling factors of Table 6 are selected such that the ratio between the factors for L_1 and L_2 and between the factors for L_2 and L_3 is kept constant. In addition, the middle scenario always contains values corresponding to the geometric mean of the two extremes. Starting from the growth kinetics Low, the growth rates of the larger characteristic lengths increase going to Medium and again to High. For breakage, Low refers to a case with no preferential breakage along any characteristic length, while Medium and High refer to progressively increased probabilities of breakage along the smaller characteristic lengths. The dissolution kinetics go from Low, a set of kinetics where the larger characteristic lengths dissolve faster, to Medium where the rates of dissolution along all characteristic lengths are the same, and to High where smaller characteristic lengths dissolve faster.

Utilizing a specific kinetics scenario outlined in Table 6, the impact of the different process parameters on the product

Table 6. List of the Nine Different Sets of Kinetics (Three Per Growth, Breakage, and Dissolution) Used for the Parametric Study[a]

growth	k_1^G/k_{ref}^G	k_2^G/k_{ref}^G	k_3^G/k_{ref}^G
Low	1.56	1.25	1
Medium	5	2.24	1
High	16	4	1
breakage	k_1^B/k_{ref}^B	k_2^B/k_{ref}^B	k_3^B/k_{ref}^B
Low	1	1	1
Medium	1	6	36
High	1	36	1296
dissolution	k_1^D/k_{ref}^D	k_2^D/k_{ref}^D	k_3^D/k_{ref}^D
Low	2.25	1.5	1
Medium	1	1	1
High	0.44	0.67	1

[a]Low, Medium, and High refer to sets of kinetics, which progressively lead to higher aspect ratios. The base values k_{ref}^G, k_{ref}^B, and k_{ref}^D are reported in Table S3 in the Supporting Information.

population is evaluated. The case with High growth and breakage kinetics and Low dissolution kinetics is used to perform 45 process simulations based on all potential permutations of the key process parameter values listed in Table 5. The results are illustrated in Figure 8, where a light gray hull delineates the area encompassing all simulated product populations. This region is subdivided by three smaller hulls, which contain the outcomes for processes with $m_D = 0.4$, $m_D = 0.2$, and $m_D = 0$, respectively. Individual simulation outcomes are indicated using circular, square, and triangular

markers representing milling intensities of $\theta = 12,000$, $\theta = 18,000$, and $\theta = 24,000$, respectively. All attained products in Figure 8a lay along the dashed line, which represents an aspect ratio $\phi_{12} = (10/3)$. In Figure 8b, a slight increase in the aspect ratio ϕ_{13} with increasing m_D can be observed. An increase in milling intensity, θ, results in a significant reduction in the average size of the product particles. Increasing the number of cycles, n_C, slightly decreases the average particle size in all scenarios.

The simulation outcomes for all 27 sets of kinetics are presented on the L_1-L_3 plane in Figure 9. An analogous representation in the L_1-L_2 plane is available in Figure S3 in the Supporting Information, showing consistent trends. However, the visual differences between simulations are more pronounced in the L_1-L_3 plane as the kinetic parameters for L_1 and L_3 are the most different. Figure 9 contains nine panels that segment the results horizontally for different dissolution parameters and vertically for different breakage parameters. Within each panel, the three corresponding scenarios with different growth parameters are visualized. Each colored hull envelopes all 45 simulations with varying process parameters. The light and dark colored areas highlight scenarios with $m_D = 0.4$ and $m_D = 0$, respectively. As the dark regions with $m_D = 0$ are not influenced by changes to the dissolution kinetics, they provide a reference for comparing results between panels with the same breakage parameters.

A key observation from Figure 9 is the narrowing of the attainable product regions and their shift toward higher aspect ratios as breakage along smaller characteristic lengths becomes more probable, regardless of the specific growth or dissolution
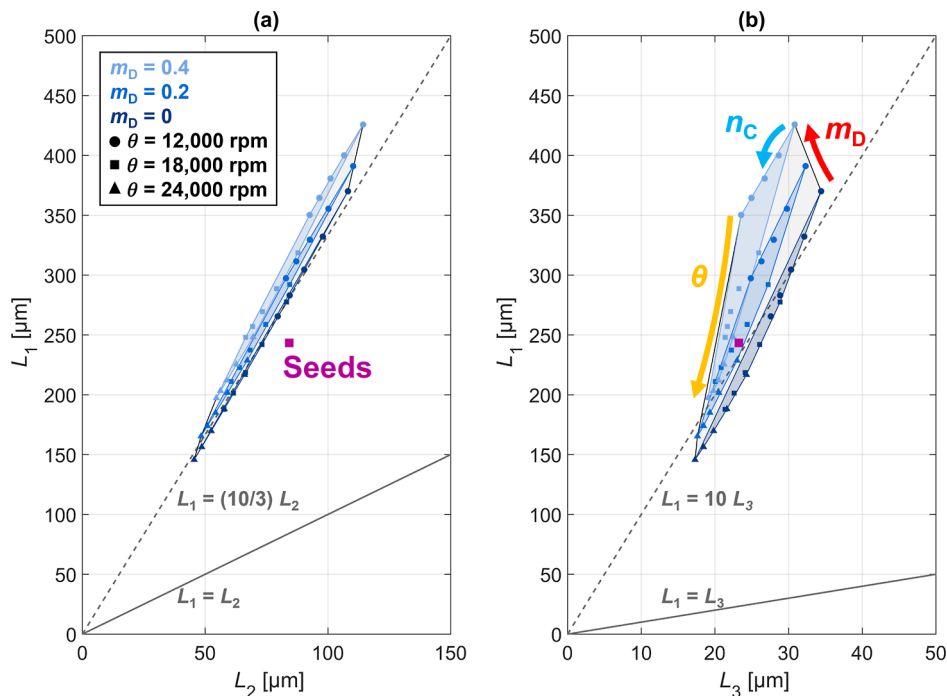

Figure 8. Visualization of the simulation results for varying key process parameters and a given set of kinetics (High growth and breakage kinetics and Low dissolution kinetics based on Table 6). (a,b) Different hulls enveloping the volume-weighted mean characteristic lengths on the L_1-L_2- and the L_1-L_3-planes, respectively. The light gray hull delineates the area encompassing all simulated product populations. This region contains three smaller hulls containing the results for processes with $m_D = 0.4$, $m_D = 0.2$, and $m_D = 0$, respectively. Individual simulation outcomes are indicated using circular, square, and triangular markers representing milling intensities of $\theta = 12,000$, $\theta = 18,000$, and $\theta = 24,000$, respectively. Both panels contain solid lines indicating a shape with all characteristic dimensions being of the same size. The dashed line in each panel represents an aspect ratio of $\phi_{12} = (10/3)$ and $\phi_{13} = 10$, respectively.
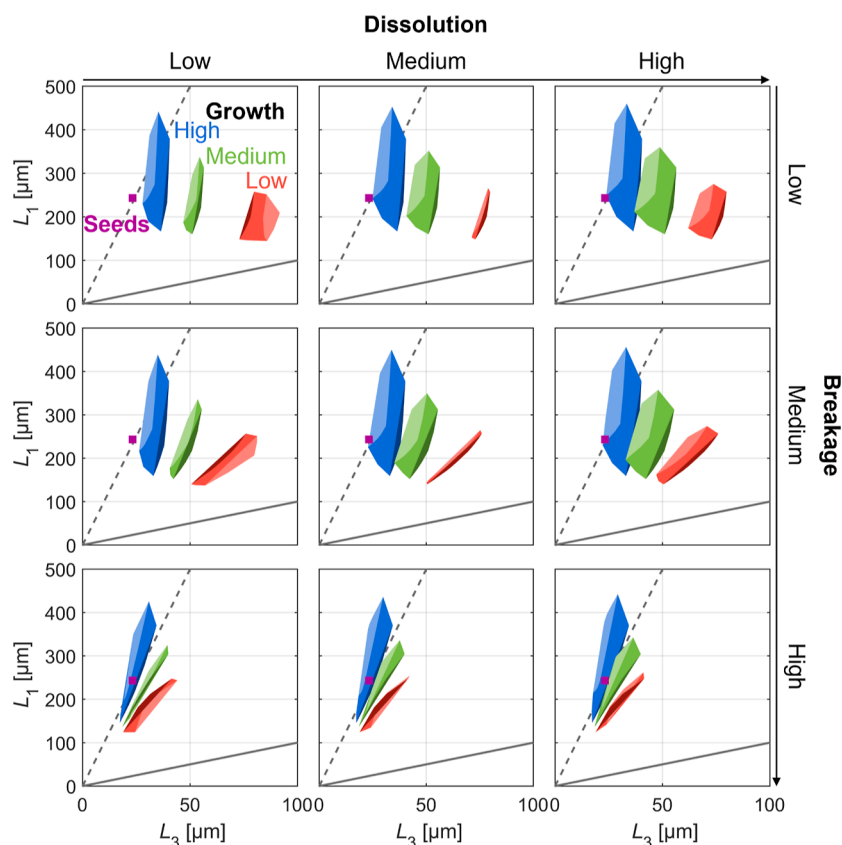
Figure 9. Visualization on the L_1-L_3 plane of the volume-weighted mean characteristic lengths of the final populations resulting from the parametric study (see Table 6 for the details about the model parameters considered). The three panels going from left to right in each row correspond to different dissolution kinetics. The three panels from top to bottom in each column show the results for different breakage kinetics. Within each of the nine panels, three different sets of growth kinetics are considered. The light and dark colored regions contain experiments with $m_D = 0.4$ and $m_D = 0$, respectively. The results of simulations in the dark regions are not affected by the dissolution kinetics and are the same in each set of horizontal figures. The solid line indicates a shape with all characteristic dimensions being of the same size. The dashed line represents an aspect ratio of $\phi_{13} = 10$. The purple square marks the seed populations.

kinetics. The growth kinetics have more influence on the position of the product region than the dissolution kinetics, especially with regard to the aspect ratio. The dissolution kinetics have a small effect on the product regions. Depending on the specific growth and dissolution kinetics, the aspect ratios reduce or increase as the fraction of mass dissolved is increased. To conclude, the findings indicate that although the multistage crystallization process can tune the absolute size of the product crystals effectively, its capacity to significantly alter the crystal shape depends strongly on the growth and breakage kinetics.

4.4. Comparison of Experimental Measurements and Simulation Results. Conclusions about the dominating phenomena within the multistage process for adipic acid can be drawn by comparing the experimentally obtained product region (Figure 3) with the results of the more general parametric simulation study (Figure 9). The kinetics of growth, breakage, and dissolution have not been measured as it is a laborious and challenging task. Therefore, such a comparison can only be qualitative, or semiquantitative at best, focusing on the relative impact of the different parameters.

The set of kinetics from the parametric study, which provides the closest match with the experiments with regard to the region of attainable product powders, can be found by first looking at the different breakage kinetics used in the simulations. The experimentally attained regions extend

along the dashed lines, which highlight specific aspect ratios, e.g., $\phi_{12} = 10/3$ and $\phi_{13} = 10$. Similar results were obtained in the parametric study for High breakage kinetics. This comparison suggests that the breakage of adipic acid crystals is significantly influenced by their crystal structure as the breakage kinetic parameter for L_3 is 3 orders of magnitude higher than for L_1.

Second, given the High breakage kinetics, the position of the experimental regions aligns the closest with the High growth kinetics. This suggests that adipic acid growth along L_1 occurs likely an order of magnitude faster than along L_3. Lastly, while the dissolution kinetics change the attainable regions little under these breakage and growth kinetics, Low dissolution kinetics provide the best match. The sets of kinetics that match the experimental results the closest are thus High growth and breakage and Low dissolution kinetics. This corresponds to the set of kinetics used to generate the results visualized in Figure 8.

One of the conclusions drawn in Section 4.3 is that the region of attainable PSSDs is mainly dependent on the breakage characteristics of the crystals. If breakage does not reduce the aspect ratios of particles, the attainable region is narrow and is only minimally dependent on the growth and dissolution kinetics. This is likely the case for adipic acid as a set of experiments in which a population of adipic acid crystals is milled at various rotor speeds, explained in detail in Section

S1.3 in the Supporting Information, shows no significant reduction in aspect ratio.

In summary, although the multistage crystallization process can influence the absolute size of adipic acid crystals, the shape of these crystals could only be changed to a small extent under the conditions of our experiments. The PBE simulation results align with the experimental measurements when one assumes that breakage is 3 orders of magnitude more likely along the smallest characteristic length than expected for a cube with no preferential breakage direction, consistent with the result of dedicated milling experiments.

5. CONCLUSIONS

By utilizing novel size and shape characterization techniques, populations of plate-like crystals were accurately characterized in suspension for the first time. This capability was subsequently utilized to systematically explore the influence of a broadly applicable multistage crystallization process on the PSSD of plate-like crystals.

First, the multistage crystallization process was applied to the model compound adipic acid in an experimental campaign. The average aspect ratios of the product crystals did not change much regardless of the operating conditions. However, the average size of and the fraction of fines in the product PSSDs were successfully modified by varying key operating conditions, namely, the number of cycles, the milling intensity, and the fraction of mass dissolved.

Increasing the fraction of mass dissolved per cycle, m_D, led to a slight increase in the aspect ratio of the product particles. This finding agrees with a previous study, where an increase in the aspect ratio of adipic acid crystals was observed when exposed to repeated growth and dissolution cycles.[27]

A complex interplay between the number of cycles, n_C, and the fraction of mass dissolved per cycle, m_D, was observed. The average particle size decreased with an increasing n_C for no dissolved mass, as reported in previous studies.[22,30,31] However, in this experimental campaign, at high fractions of mass dissolved, e.g., $m_D = 0.4$, the particle size significantly increased at the higher n_C. A likely explanation for this observation is that the breakage rate of adipic acid is much lower compared to previously investigated compounds (β L-glutamic acid and γ D-mannitol) under comparable conditions.[22,30,31] This low breakage frequency likely leads to a regime where the particle count decreases from cycle to cycle due to dissolution removing more particles than what was generated during milling. This leads to more mass per particle per cycle and thus to an increasing average particle size. This explanation could be verified if the evolution of the PSSD was tracked, which was not possible because of a lack of an effective tool to measure the PSSD in suspensions with high particle densities, as in this case.

Second, the filter cake resistances of accurately characterized crystal populations of plate-like particles were measured, thus demonstrating the potential improvements in the downstream processability of the product crystals through an optimal design of the crystallization process. The results indicate a significant reduction of the filter cake resistance as the average particle size increases and the fines fraction is reduced. These findings match results previously reported for needle-like compounds.[36]

Third, a modeling framework, containing multiple morphological population balance equation models, was used to understand the evolution of the PSSD through the multistage process. This model was subsequently used to conduct a comprehensive characterization of the process's PSSD modification capabilities under various conditions and for a diverse set of kinetics. The studies revealed that the growth and dissolution kinetics of the crystals are of secondary importance regarding the crystal shape if crystal breakage produces particles with high aspect ratios.

The good qualitative match between the experimental and simulation studies underscores the importance of a combined experimental and modeling approach when designing crystallization processes. Ideally, efforts should be invested in experimentally estimating growth, dissolution, and breakage kinetics with the least experimental effort. This would allow for the use of modeling frameworks to rapidly evaluate the efficacy of the multistage process for shape manipulation. This approach would allow for quick screening of process alternatives, saving time and resources compared to process development without the aid of modeling.

Based on the size and shape engineering strategies previously developed for needle-like particles,[21,22,32,48] here, we have expanded the characterization capabilities, experimental techniques, and modeling frameworks to plate-like crystals. The modification of the PSSD of plate-like crystals, and with it the adjustment of the product properties for downstream processing, has been successfully achieved. While the degree of shape manipulation achieved is not as significant as in previous studies on needle-like compounds, this work has illuminated the complexities and opportunities for future investigations into crystallization processes designed specifically for plate-like crystals.

■ ASSOCIATED CONTENT

ⓈI Supporting Information

The Supporting Information is available free of charge at https://pubs.acs.org/doi/10.1021/acs.cgd.4c00277.

> Additional information about the particle size and shape distribution of the seed population for both the simulations and experiments; deagglomeration experiment using the wet mill; dedicated wet milling experiment to assess the breakage behavior of adipic acid; additional details about the growth, dissolution, and breakage PBE models; and additional visualizations of the results of the parametric study (PDF)

■ AUTHOR INFORMATION

Corresponding Author

Marco Mazzotti − *Institute of Energy and Process Engineering, ETH Zurich, 8092 Zurich, Switzerland;* ⓞ orcid.org/0000-0002-4948-6705; Phone: +41 44 632 24 56; Email: marco.mazzotti@ipe.mavt.ethz.ch

Authors

Daniel Biri − *Institute of Energy and Process Engineering, ETH Zurich, 8092 Zurich, Switzerland;* ⓞ orcid.org/0009-0003-8195-4884

Anna Jaeggi − *Institute of Energy and Process Engineering, ETH Zurich, 8092 Zurich, Switzerland*

Pavel Malach − *Institute of Energy and Process Engineering, ETH Zurich, 8092 Zurich, Switzerland*

Ashwin Kumar Rajagopalan − *Department of Chemical Engineering, The University of Manchester, M13 9PL Manchester, U.K.;* ⓞ orcid.org/0000-0001-8306-455X

Complete contact information is available at:
https://pubs.acs.org/10.1021/acs.cgd.4c00277

■ NOTATION

A	filtration area $[\text{m}^2]$
B	birth term $[\mu m\ \text{kg}^{-3}\ \text{s}]$
c	solute concentration in the liquid phase $[\text{g kg}^{-1}]$
c_0	initial solute concentration in the liquid phase $[\text{g kg}^{-1}]$
$c*$	solubility $[\text{g kg}^{-1}]$
D_i	dissolution rate in L_i direction $[\mu m\ \text{s}^{-1}]$
E	death term $[\mu m\ \text{kg}^{-3}\ \text{s}]$
F	pump flow rate $[\text{L min}^{-1}]$
f	number density function $[\mu m^{-3}\ \text{kg}^{-1}]$
G_i	growth rate in L_i direction $[\mu m\ \text{s}^{-1}]$
K_i	breakage frequency in L_i direction $[\text{s}^{-1}]$
k	cake permeability $[\text{m}^2]$
k_v	shape factor $[\text{-}]$
L_i	crystal characteristic dimension i $[\mu m]$
$L_{i,n}$	number-weighted average characteristic dimension i $[\mu m]$
$L_{i,v}$	volume-weighted average characteristic dimension i $[\mu m]$
m_C	mass of the filter cake $[\text{kg}]$
ΔP	pressure drop over the filter cake $[\text{Pa}]$
Q_v	volumetric flow rate during filtration $[\text{m}^3\ \text{s}^{-1}]$
S	supersaturation $[\text{-}]$
t	time $[\text{s}]$
T	temperature $[°\text{C}]$
α_m	filter cake resistance $[\text{m kg}^{-1}]$
β	blank resistance $[\text{m}^{-1}]$
γ_c	cooling rate $[\text{K h}^{-1}]$
γ_h	heating rate $[\text{K h}^{-1}]$
Γ_i	growth/dissolution rate in L_i direction $[\mu m\ \text{s}^{-1}]$
θ	wet mill rotor speed $[\text{rpm}]$
μ	dynamic viscosity $[\text{Pa s}]$
μ_{ijk}	cross moment ijk of the PSSD $[\text{varies}]$
ρ	density of the crystalline phase $[\text{kg m}^{-3}]$
τ	residence time in the wet mill $[\text{s}]$
ϕ_{ij}	aspect ratio L_i/L_j $[-]$

■ REFERENCES

(1) Pudasaini, N.; Upadhyay, P. P.; Parker, C. R.; Hagen, S. U.; Bond, A. D.; Rantanen, J. Downstream Processability of Crystal Habit-Modified Active Pharmaceutical Ingredient. *Org. Process Res. Dev.* **2017**, *21*, 571−577.

(2) Azad, M. A.; Capellades, G.; Wang, A. B.; Klee, D. M.; Hammersmith, G.; Rapp, K.; Brancazio, D.; Myerson, A. S. Impact of Critical Material Attributes (CMAs)-Particle Shape on Miniature Pharmaceutical Unit Operations. *AAPS PharmSciTech* **2021**, *22*, 98.

(3) Khadka, P.; Ro, J.; Kim, H.; Kim, I.; Kim, J. T.; Kim, H.; Cho, J. M.; Yun, G.; Lee, J. Pharmaceutical particle technologies: An approach to improve drug solubility, dissolution and bioavailability. *Asian J. Pharm. Sci.* **2014**, *9*, 304−316.

(4) Chatterjee, A.; Gupta, M.; Srivastava, B. Spherical crystallization: A technique use to reform solubility and flow property of active pharmaceutical ingredients. *Int. J. Pharm. Invest.* **2017**, *7*, 4−9.

(5) Chow, K.; Tong, H. H.; Lum, S.; Chow, A. H. Engineering of Pharmaceutical Materials: An Industrial Perspective. *J. Pharm. Sci.* **2008**, *97*, 2855−2877.

(6) Variankaval, N.; Cote, A. S.; Doherty, M. F. From form to function: Crystallization of active pharmaceutical ingredients. *Cryst. Growth Des.* **2008**, *54*, 1682−1688.

(7) Rasenack, N.; Müller, B. W. Ibuprofen crystals with optimized properties. *Int. J. Pharm.* **2002**, *245*, 9−24.

(8) Heng, J. Y.; Bismarck, A.; Lee, A. F.; Wilson, K.; Williams, D. R. Anisotropic Surface Chemistry of Aspirin Crystals. *J. Pharm. Sci.* **2007**, *96*, 2134−2144.

(9) El-Zhry El-Yafi, A. K.; El-Zein, H. Technical crystallization for application in pharmaceutical material engineering: Review article. *Asian J. Pharm. Sci.* **2015**, *10*, 283−291.

(10) Wakeman, R. The influence of particle properties on filtration. *Sep. Purif. Technol.* **2007**, *58*, 234−241.

(11) Bourcier, D.; Féraud, J.; Colson, D.; Mandrick, K.; Ode, D.; Brackx, E.; Puel, F. Influence of particle size and shape properties on cake resistance and compressibility during pressure filtration. *Chem. Eng. Sci.* **2016**, *144*, 176−187.

(12) Pu, S.; Hadinoto, K. Habit modification in pharmaceutical crystallization: A review. *Chem. Eng. Res. Des.* **2024**, *201*, 45−66.

(13) Nokhodchi, A.; Bolourtchian, N.; Dinarvand, R. Crystal modification of phenytoin using different solvents and crystallization conditions. *Int. J. Pharm.* **2003**, *250*, 85−97.

(14) Simone, E.; Steele, G.; Nagy, Z. K. Tailoring crystal shape and polymorphism using combinations of solvents and a structurally related additive. *Cryst. Eng. Comm* **2015**, *17*, 9370−9379.

(15) Hatcher, L. E.; Li, W.; Payne, P.; Benyahia, B.; Rielly, C. D.; Wilson, C. C. Tuning Morphology in Active Pharmaceutical Ingredients: Controlling the Crystal Habit of Lovastatin through Solvent Choice and Non-Size-Matched Polymer Additives. *Cryst. Growth Des.* **2020**, *20*, 5854−5862.

(16) Amaro-González, D.; Biscans, B. Spherical agglomeration during crystallization of an active pharmaceutical ingredient. *Powder Technol.* **2002**, *128*, 188−194.

(17) Abu Bakar, M. R.; Nagy, Z. K.; Saleemi, A. N.; Rielly, C. D. The Impact of Direct Nucleation Control on Crystal Size Distribution in Pharmaceutical Crystallization Processes. *Cryst. Growth Des.* **2009**, *9*, 1378−1384.

(18) Eisenschmidt, H.; Bajcinca, N.; Sundmacher, K. Optimal Control of Crystal Shapes in Batch Crystallization Experiments by Growth-Dissolution Cycles. *Cryst. Growth Des.* **2016**, *16*, 3297−3306.

(19) Kumar, D.; Worku, Z. A.; Gao, Y.; Kamaraju, V. K.; Glennon, B.; Babu, R. P.; Healy, A. M. Comparison of wet milling and dry milling routes for ibuprofen pharmaceutical crystals and their impact on pharmaceutical and biopharmaceutical properties. *Powder Technol.* **2018**, *330*, 228−238.

(20) Szilágyi, B.; Nagy, Z. K. Population Balance Modeling and Optimization of an Integrated Batch Crystallizer − Wet Mill System for Crystal Size Distribution Control. *Cryst. Growth Des.* **2018**, *18*, 1415−1424.

(21) Bötschi, S.; Rajagopalan, A. K.; Rombaut, I.; Morari, M.; Mazzotti, M. From needle-like toward equant particles: A controlled crystal shape engineering pathway. *Comput. Chem. Eng.* **2019**, *131*, 106581.

(22) Salvatori, F.; Binel, P.; Mazzotti, M. Efficient assessment of combined crystallization, milling, and dissolution cycles for crystal size and shape manipulation. *Chem. Eng. Sci.* **2019**, *1*, 100004.

(23) Eren, A.; Szilagyi, B.; Quon, J. L.; Papageorgiou, C. D.; Nagy, Z. K. Experimental Investigation of an Integrated Crystallization and Wet-Milling System with Temperature Cycling to Control the Size and Aspect Ratio of Needle-Shaped Pharmaceutical Crystals. *Cryst. Growth Des.* **2021**, *21*, 3981−3993.

(24) Jaeggi, A.; Rajagopalan, A. K.; Morari, M.; Mazzotti, M. Characterizing Ensembles of Platelike Particles via Machine Learning. *Ind. Eng. Chem. Res.* **2021**, *60*, 473−483.

(25) Binel, P.; Jain, A.; Jaeggi, A.; Biri, D.; Rajagopalan, A. K.; deMello, A. J.; Mazzotti, M. Online 3D Characterization of

Micrometer-Sized Cuboidal Particles in Suspension. *Small Methods* **2023**, *7*, 2201018.

(26) Brown, C. J.; Lee, Y. C.; Nagy, Z.; Ni, X. Evaluation of crystallization kinetics of adipic acid in an oscillatory baffled crystallizer. *CrystEngComm* **2014**, *16*, 8008−8014.

(27) Lovette, M. A.; Muratore, M.; Doherty, M. F. Crystal shape modification through cycles of dissolution and growth: Attainable regions and experimental validation. *AIChE J.* **2012**, *58*, 1465−1474.

(28) Ramkrishna, D. *Population Balances: Theory and Applications of Particulate Systems in Engineering*, Elsevier, 2000; p 355.

(29) Gunawan, R.; Fusman, I.; Braatz, R. D. High Resolution Algorithms for Multidimensional Population Balance Equations. *AIChE J.* **2004**, *50*, 2738−2749.

(30) Salvatori, F.; Mazzotti, M. Manipulation of Particle Morphology by Crystallization, Milling, and Heating Cycles-A Mathematical Modeling Approach. *Ind. Eng. Chem. Res.* **2017**, *56*, 9188−9201.

(31) Salvatori, F.; Mazzotti, M. Manipulation of Particle Morphology by Crystallization, Milling, and Heating Cycles: Experimental Characterization. *Ind. Eng. Chem. Res.* **2018**, *57*, 15522−15533.

(32) Salvatori, F.; Mazzotti, M. Experimental Characterization and Mathematical Modeling of Breakage of Needle-like Crystals in a Continuous Rotor-Stator Wet Mill. *Cryst. Growth Des.* **2018**, *18*, 5957−5972.

(33) Rajagopalan, A. K.; Bötschi, S.; Morari, M.; Mazzotti, M. Feedback Control for the Size and Shape Evolution of Needle-like Crystals in Suspension. III. Wet Milling. *Cryst. Growth Des.* **2019**, *19*, 2845−2861.

(34) Ho, R.; Naderi, M.; Heng, J. Y.; Williams, D. R.; Thielmann, F.; Bouza, P.; Keith, A. R.; Thiele, G.; Burnett, D. J. Effect of milling on particle shape and surface energy heterogeneity of needle-shaped crystals. *Pharm. Res.* **2012**, *29*, 2806−2816.

(35) Grof, Z.; Schoellhammer, C. M.; Rajniak, P.; Stepanek, F. Computational and experimental investigation of needle-shaped crystal breakage. *Int. J. Pharm.* **2011**, *407*, 12−20.

(36) Perini, G.; Salvatori, F.; Ochsenbein, D. R.; Mazzotti, M.; Vetter, T. Filterability prediction of needle-like crystals based on particle size and shape distribution data. *Sep. Purif. Technol.* **2019**, *211*, 768−781.

(37) Binel, P.; Mazzotti, M. Improving the Performance of a 3-Stage Cyclic Crystallization Process Using a Hydrocyclone. *Ind. amp; Eng. Chem. Res.* **2022**, *61*, 16220−16232.

(38) Narducci, O.; Jones, A.; Kougoulos, E. Continuous crystallization of adipic acid with ultrasound. *Chem. Eng. Sci.* **2011**, *66*, 1069−1076.

(39) Klapwijk, A. R.; Simone, E.; Nagy, Z. K.; Wilson, C. C. Tuning Crystal Morphology of Succinic Acid Using a Polymer Additive. *Cryst. Growth Des.* **2016**, *16*, 4349−4359.

(40) Simone, E.; Klapwijk, A. R.; Wilson, C. C.; Nagy, Z. K. Investigation of the Evolution of Crystal Size and Shape during Temperature Cycling and in the Presence of a Polymeric Additive Using Combined Process Analytical Technologies. *Cryst. Growth Des.* **2017**, *17*, 1695−1706.

(41) Vetter, T.; Mazzotti, M.; Brozio, J. Slowing the Growth Rate of Ibuprofen Crystals Using the Polymeric Additive Pluronic F127. *Cryst. Growth Des.* **2011**, *11*, 3813−3821.

(42) Gaivoronskii, A. N.; Granzhan, V. A. Solubility of Adipic Acid in Organic Solvents and Water. *Russ. J. Appl. Chem.* **2005**, *78*, 404−408.

(43) Mao, Z.; Sun, X.; Luan, X.; Wang, Y.; Liu, G. Measurement and Correlation of Solubilities of Adipic Acid in Different Solvents. *Chin. J. Chem. Eng.* **2009**, *17*, 473−477.

(44) Rajagopalan, A. K.; Schneeberger, J.; Salvatori, F.; Bötschi, S.; Ochsenbein, D. R.; Oswald, M. R.; Pollefeys, M.; Mazzotti, M. A comprehensive shape analysis pipeline for stereoscopic measurements of particulate populations in suspension. *Powder Technol.* **2017**, *321*, 479−493.

(45) Ripperger, S.; Gösele, W.; Alt, C.; Loewe, T. *Ullmann's Encyclopedia of Industrial Chemistry*; John Wiley & Sons, Ltd, 2013; pp 1−38.

(46) de Albuquerque, I.; Mazzotti, M.; Ochsenbein, D. R.; Morari, M. Effect of needle-like crystal shape on measured particle size distributions. *AIChE J.* **2016**, *62*, 2974−2985.

(47) Kumar, S.; Ramkrishna, D. On the solution of population balance equations by discretization — I. A fixed pivot technique. *Chem. Eng. Sci.* **1996**, *51*, 1311−1332.

(48) Bötschi, S.; Rajagopalan, A. K.; Morari, M.; Mazzotti, M. Feedback Control for the Size and Shape Evolution of Needle-like Crystals in Suspension. IV. Modeling and Control of Dissolution. *Cryst. Growth Des.* **2019**, *19*, 4029−4043.